

Ground-based estimates of outer radiation belt energetic electron precipitation fluxes into the atmosphere

Mark A. Clilverd,¹ Craig J. Rodger,² Rory J. Gamble,² Thomas Ulich,³ Tero Raita,³ Annika Seppälä,^{1,4} Janet C. Green,⁵ Neil R. Thomson,² Jean-André Sauvaud,⁶ and Michel Parrot⁷

Received 4 May 2010; revised 30 June 2010; accepted 22 July 2010; published 4 December 2010.

[1] AARDDVARK data from a radio wave receiver in Sodankylä, Finland have been used to monitor transmissions across the auroral oval and just into the polar cap from the very low frequency communications transmitter, call sign NAA (24.0 kHz, 44°N, 67°W, $L = 2.9$), in Maine, USA, since 2004. The transmissions are influenced by outer radiation belt ($L = 3-7$) energetic electron precipitation. In this study, we have been able to show that the observed transmission amplitude variations can be used to determine routinely the flux of energetic electrons entering the upper atmosphere along the total path and between 30 and 90 km. Our analysis of the NAA observations shows that electron precipitation fluxes can vary by 3 orders of magnitude during geomagnetic storms. Typically when averaging over $L = 3-7$ we find that the >100 keV POES “trapped” fluxes peak at about 10^6 el. $\text{cm}^{-2} \text{s}^{-1} \text{sr}^{-1}$ during geomagnetic storms, with the DEMETER >100 keV drift loss cone showing peak fluxes of 10^5 el. $\text{cm}^{-2} \text{s}^{-1} \text{sr}^{-1}$, and both the POES >100 keV “loss” fluxes and the NAA ground-based >100 keV precipitation fluxes showing peaks of $\sim 10^4$ el. $\text{cm}^{-2} \text{s}^{-1} \text{sr}^{-1}$. During a geomagnetic storm in July 2005, there were systematic MLT variations in the fluxes observed: electron precipitation flux in the midnight sector (22–06 MLT) exceeded the fluxes from the morning side (0330–1130 MLT) and also from the afternoon sector (1130–1930 MLT). The analysis of NAA amplitude variability has the potential of providing a detailed, near real-time, picture of energetic electron precipitation fluxes from the outer radiation belts.

Citation: Clilverd, M. A., C. J. Rodger, R. J. Gamble, T. Ulich, T. Raita, A. Seppälä, J. C. Green, N. R. Thomson, J.-A. Sauvaud, and M. Parrot (2010), Ground-based estimates of outer radiation belt energetic electron precipitation fluxes into the atmosphere, *J. Geophys. Res.*, *115*, A12304, doi:10.1029/2010JA015638.

1. Introduction

[2] Currently, there is intense debate as to the ultimate effects of solar activity on tropospheric and stratospheric variability, particularly through direct and indirect effects of chemical changes induced by energetic particle precipitation [Randall *et al.*, 2005; Rozanov *et al.*, 2005; Seppälä *et al.*, 2009]. In this study, we investigate a ground-based technique to make estimates of energetic particles precipitating into the Earth’s atmosphere. The precipitating particles ionize the neutral atmosphere, consequently changing atmospheric

chemistry, and modifying the radiation balance. Recently Seppälä *et al.* [2009] used the ERA40 reanalysis data set from 1957 to 2006 to confirm the linkage between geomagnetic activity variations and substantial wintertime (December–February in the Northern Hemisphere) surface temperature variations in the polar regions. Seppälä *et al.* found that polar surface–air temperatures in years with high average Ap index levels were different than in years with low Ap index; the differences were statistically significant at the 2 sigma level and range up to about ± 4.5 K, depending on location within the polar regions. The analysis of Seppälä *et al.* suggests that the most likely mechanism connecting geomagnetic activity and surface temperature is the modification of the chemical composition of the upper atmosphere resulting from energetic particle precipitation from space. Previously, this linkage had been suggested by coupled climate modeling results published by Rozanov *et al.* [2005], using the UIUC CCM and two 10 year runs, with and without geomagnetic forcing of upper atmospheric chemistry. The variation in polar surface temperatures between extremes of geomagnetic activity is ± 4 K in both the model predictions and the data analysis. The effects are clearly significant

¹British Antarctic Survey, Natural Environment Research Council, Cambridge, UK.

²Department of Physics, University of Otago, Dunedin, New Zealand.

³Sodankylä Geophysical Observatory, University of Oulu, Sodankylä, Finland.

⁴Earth Observation, Finnish Meteorological Institute, Helsinki, Finland.

⁵Space Weather Prediction Center, NOAA, Boulder, Colorado, USA.

⁶Centre d’Etude Spatiale des Rayonnements, Toulouse, France.

⁷Laboratoire de Physique et Chimie de l’Environnement et de l’Espace, Orleans, France.

in terms of natural polar temperature variability and need to be understood in detail.

[3] However, there are key unresolved questions concerning the understanding of the effects of energetic particle precipitation on the lower atmosphere: (1) What are the main characteristics of the particle precipitation? (2) What are the key chemical changes in the upper atmosphere? (3) How are these chemical changes transported/coupled to the lower atmosphere? (4) What is the contribution of energetic particle-induced upper atmosphere chemical modification to stratospheric chemistry as a whole? To help answer these fundamental questions, this paper aims to ascertain the temporal and spatial variability of precipitating radiation belt energetic electrons. Definitive answers are very difficult to provide from satellite measurements alone because of the complexity in measuring electron fluxes unambiguously in the whole bounce-loss cone (BLC) without contamination from fluxes in the drift-loss cone (DLC) or trapped fluxes [e.g., *Rodger et al.*, 2010]. In current atmospheric modeling efforts, which include an energetic particle precipitation effect, a proxy for the precipitation (such as a geomagnetic activity index like A_p) is sometimes used instead [e.g., *Baumgaertner et al.*, 2009]. By determining the actual precipitating particle characteristics, it will be possible to undertake more definitive modeling of the atmospheric chemistry changes driven by particle precipitation and hence more definitive modeling of the whole process.

[4] Within the Earth's protective magnetic field populations of electrons are trapped, energized, transported, and lost from the radiation belts by processes such as ULF and VLF wave-particle interactions [*Horne et al.*, 2005; *Rodger and Clilverd*, 2008]. These processes tend to have a maximum effect in the "heart of the radiation belts" at $L \sim 4-5$ (geomagnetic latitude $60^\circ-63^\circ$) but stretch over the whole of the outer radiation belt from $L \sim 3-8$ (geomagnetic latitude $54^\circ-71^\circ$). At geostationary orbits, geomagnetic storms have been found to cause significant variations in trapped radiation belt relativistic electron fluxes, through a complex interplay between competing acceleration and loss mechanisms. *Reeves* [1998] found that geomagnetic storms produce all possible responses in the outer belt flux levels, i.e., flux increases (53%), flux decreases (19%), and no change (28%). Understanding the loss of relativistic electrons is a key part to understanding the dynamics of the energetic radiation belts. The impact of electrons precipitating from the radiation belts is to drive chemical changes in the polar atmosphere, particularly the production of odd nitrogen, which potentially survives over long-time scales, and is generated over large geographical areas depending on the wave-particle processes that are occurring at the time.

[5] Ground based Antarctic-Arctic Radiation-belt Dynamic Deposition VLF Atmospheric Research Konsortia (AARDDVARK) observations (see *Clilverd et al.* [2009a] for a summary) of the modification of radio communications by energetic electron precipitation have, up to now, focused on the investigation and understanding of precipitation events associated with short-lived bursts of electrons [*Rodger et al.*, 2007a; *Rodger et al.*, 2008; *Clilverd et al.*, 2006] or single large storms [*Rodger et al.*, 2007b; *Clilverd et al.*, 2009b]. However, the analysis undertaken indicates that AARDDVARK observations should be able to provide longer-term monitoring of electron fluxes. The development of a tech-

nique to monitor energetic electron precipitation into the atmosphere will be timely in that during the up coming cycle 24 solar maximum detailed measurements of radiation belt processes and dynamics will be made by multiple satellite missions: NASA's RBSP twin satellites due to be launched in 2012 as part of the Living With a Star Geospace mission, the Japanese ERG mission to be launched in 2012, and the Canadian Space Agency's ORBITALS due to be launched in 2014. RBSP (Radiation Belt Storm Probes) aims to discover the fundamental physics underlying the source, loss, and transport processes that govern the radiation belts.

[6] Here we make use of AARDDVARK data from a radio wave receiver in Sodankylä, Finland, which has been monitoring transmissions from the very low frequency naval transmitter, NAA, in Cutler, Maine, USA since 2004. We show that the amplitude variations, outside of the normal diurnal variations exhibited by the received signal, are primarily driven by electron precipitation associated with geomagnetic storms and can be compared with electron fluxes detected by the POES and DEMETER satellites. We further model the amplitude variations in order to determine an integral electron precipitation flux which represents the ionization along the total path for specific times of day and limited ranges of MLT.

2. Experimental Setup

[7] The AARDDVARK network currently uses narrow band subionospheric VLF/LF data spanning 10–40 kHz. Receiver sites are part of the Antarctic-Arctic Radiation-belt Dynamic Deposition VLF Atmospheric Research Konsortia [*Clilverd et al.*, 2009a] or AARDDVARK. Each receiver is capable of receiving multiple narrowband transmissions from powerful man-made communication transmitters. This study makes use of the transmissions from NAA (24.0 kHz, 44°N , 67°W , $L = 2.9$) received at Sodankylä (SGO, 67°N , 26°E , $L = 5.1$). The great circle path (GCP) is shown in Figure 1 as a solid line and is 5652 km long. Also plotted are the L shell contours for $L = 3, 5$, and 7 . The plot shows that the NAA to SGO GCP is orientated in such a way that can be influenced by energetic particle precipitation from $L \sim 3-8$. The effects of changing propagation conditions in the mesosphere, often due to energetic particle precipitation can be seen as either an increase or decrease in signal amplitude or phase depending on the modal mixture of each signal observed [*Barr et al.*, 2000].

[8] The OmniPAL narrowband VLF receiver operation was described by *Clilverd et al.* [2009a], which includes the details of the receiver operation. However, we note here that the SGO OmniPAL is a software defined radio (SDR) system [*Adams and Dowden*, 1990] able to receive up to 6 VLF transmissions, and at SGO the received amplitude and phase values are averaged over an interval of 0.1 s. However, in this study we make use of a processed data set that comprises 1 min median amplitude values.

[9] To compare with the ground-based observations we also make use of particle measurements by the Space Environment Monitor 2 instrument packages onboard the POES spacecraft, which are in Sun-synchronous orbits at $\sim 800-850$ km altitudes. SEM-2 includes the Medium Energy Proton and Electron Detector (MEPED), in addition to the Total Energy Detector (TED). Together, these instruments

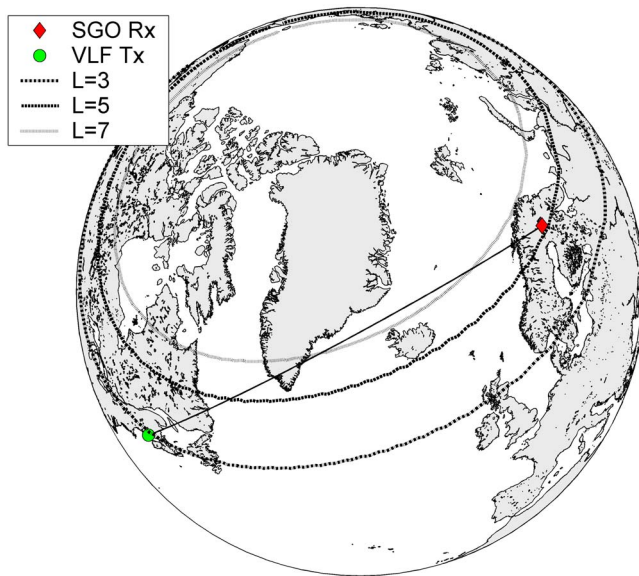


Figure 1. A map of the subionospheric VLF propagation path from the NAA transmitter (circle) to the SGO receiver in Finland (diamond). Contours of constant L shell are shown for $L = 3, 5,$ and 7 .

monitor electron fluxes from 50 eV up to 2500 keV [Evans and Greer, 2004; Rodger et al., 2010]. All POES data are available from <http://poes.ngdc.noaa.gov/data/>; while the full-resolution data has 1 s measurements at a 2 s cadence, we work with the 16 s resolution ASCII files. Analysis of POES data for this study focuses primarily on the electrons that are trapped in the Van Allen radiation belts, and we specifically average the fluxes between $L = 3-7$ in order to compare them with the results from the NAA to SGO radio wave data. We consider observations from both the “trapped” (90° detector) and “loss” (0° detector) >100 keV telescopes (e2), after removing contamination from low-energy protons [Rodger et al., 2010].

[10] Additional analysis and comparison is made with the DETEMER satellite electron fluxes. DEMETER is the first of the Myriade series of microsatellites developed by the Centre National d’Etudes Spatiales for low-cost science missions and was placed in a circular Sun-synchronous polar orbit at an altitude of 710 km at the end of June 2004. The IDP spectrometer [Sauvaud et al., 2006] primarily measures drift loss cone electron fluxes and is unusual in that it has very high energy resolution; even in its normal “survey” mode the instrument resolves energies from 70 keV to 2.34 MeV using 128 energy channels. We make use of the high-energy resolution data from DEMETER to determine the average energy spectrum of electrons in the $L = 3-7$ range and use that as an input into the modeling of the effect of electron precipitation on the NAA to SGO propagation path.

3. Results

[11] The OmniPAL receiver was installed at Sodankylä in late November 2004 and has operated as near to continuously as possible until the present day. Some data gaps were

caused by occasional instrumental failures, and there were also two periods when the aerial system was temporarily moved to Kilpisjärvi (October 2006 and October 2007). The NAA amplitudes were checked and recalibrated after each period of failure or movement as part of the initial phase of this study. Figure 2 shows the 1 min resolution median amplitudes of the NAA transmitter observed from Sodankylä, Finland, during the period December 2004 to May 2009. The range of colors represents the amplitude of the received signal in dB relative to an arbitrary voltage. Variations in intensity occur during the times of sunrise conditions at NAA (labeled SR NAA) and sunset at NAA (labeled SS NAA) as a result of rapidly changing propagation conditions. The equivalent times of sunrise and sunset at Sodankylä are not so clearly identified in this plot and have not been labeled. Although the effects of sunrise/sunset at NAA are easy to pick out in Figure 2, it should be noted that the amplitude received at SGO is representative of the ionization levels along the total path and not just at the location of the transmitter. The timing of the substantial amplitude minima/maxima is consistent with modal conversion taking place as the sunrise/sunset terminator passes overhead of the transmitter [Clilverd et al., 1999]. Red-yellow horizontal stripes typically indicate variations in signal amplitude as a result of changing propagation conditions, often caused by geomagnetic storm-induced energetic particle precipitation. The appearance of these horizontal bands of enhanced amplitude at all times of the day and year is clear evidence that the particle precipitation is widely distributed over the whole propagation path and not confined to a small spatial region as with the sunrise/sunset effects. It is these enhanced amplitude features that we study in this paper. A period of blue coloring in November–December 2008 at $\sim 02-03$ UT was caused by the NAA transmitter undergoing a series of short pulsed transmissions which affect the 1 min medians. White horizontal stripes indicate periods when the transmitter was off or when the Sodankylä receiver system was not operating.

[12] In Figure 3, we show UT time slices of some of the data shown in Figure 2. The panels show the variation of the amplitude of the transmissions from NAA received at Sodankylä for three 1 h time periods during 2005 (solid line). From top to bottom, we plot the 02–03 UT time period, which because of the length of the great circle path corresponds to 22–06 MLT, i.e., the midnight sector; the 08–09 UT period (0330–1130 MLT, morning sector); and the 16–17 UT period (the 1130–1930 MLT, afternoon sector). The dash-dotted lines represent the variation of quiet time amplitude values during the year based on the analysis of data from 2005 to 2008 during truly quiet time periods, i.e., with minimal contributions from electron precipitation effects. Although days of true quiet only occur infrequently, e.g., days 20, 80, 115, and 140 in Figure 3 (top), by over-laying the data from all 4 years we were able to increase the occurrence frequency of these events throughout the year. As a result, the quiet time values shown are representative of the accumulated picture from all 4 years of data. As a general rule, the quiet time values are higher during the summer months (between days 140 and 260) and lower during the winter. However, different times of day show different variations in baseline values depending on the influence of sunrise and sunset conditions on the great circle

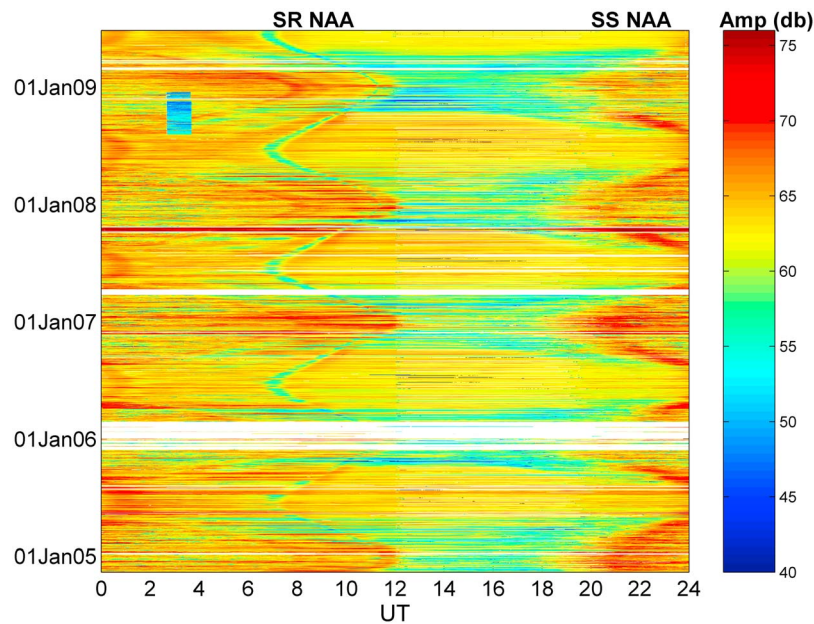


Figure 2. One minute resolution median amplitudes of the NAA transmitter observed from Sodankylä, Finland during the period December 2004 to May 2009. The range of colors represents the amplitude of the received signal in dB relative to an arbitrary voltage. Labels identify the times when the amplitudes are influenced by propagation conditions associated with sunrise (SR) and sunset (SS) at NAA. The positions of the SS and SR labels broadly identify these periods. Sunrise/sunset effects appear as short-lived changes in amplitude (increases or decreases) that exhibit a seasonal dependence. The equivalent SGO SR and SS features are less easy to pick out in this plot.

path between the transmitter and the receiver. For example, the dip in baseline values at day 225 in the 0800 UT panel is caused by a well-defined modal minimum associated with the time of sunrise at the NAA transmitter (see Figure 2). During the summer months, all time periods shown have baseline values that are the same (i.e., ~ 60.5 dB in these panels). Deviations away from the quiet time values are typically seen as an increase in amplitude. The largest amplitudes observed are typically about 70 dB, which represents an ~ 9 – 10 dB enhancement on the maximum baseline values of ~ 60.5 dB.

[13] An example of the response of the NAA amplitude to periods of enhanced geomagnetic activity and elevated radiation belt energetic electron fluxes is shown in Figure 4. The variation in daily mean A_p (top), NAA amplitude (middle) and POES >100 keV trapped electron counts averaged over $L = 3$ – 7 (bottom) are shown during the equinox period from day 60 to day 170 (2006). Vertical dashed lines are plotted to highlight examples of geomagnetic storm periods as defined by A_p and their corresponding signatures in NAA amplitudes and POES electron counts. The NAA amplitude responds to the geomagnetic storms with increased amplitude compared with the quiet time values indicated by the dot-dashed line. The POES >100 keV trapped fluxes also show increases in response to the geomagnetic storms. Although the sequence of three short-lived geomagnetic storms that start on day 93 are well separated in A_p (which indicates the onset of particle precipitation but not the amount or duration), the NAA

response and the POES electron counts both show elevated levels for the entire period through to day ~ 120 .

[14] A further example of the response of NAA amplitudes to periods of enhanced geomagnetic activity is shown in Figure 5. In Figure 5 (top), the variation of NAA amplitude (solid line) during days 118–180 (2005) at 0230 UT is compared with daily A_p (dotted line). The quiet time baseline values for NAA at this time of year are indicated by the dot-dashed line. Increases in the amplitude of NAA occur in response to increases in A_p but are typically delayed by a day or so often last longer than the disturbance in A_p and sometimes show significant responses to only small changes in A_p . Examples of each of these types of behavior are identified by two vertical dashed lines. In Figure 5 (bottom), the POES >100 keV trapped electron counts (average over $L = 3$ – 7) are shown during the same period as at the top. Variations in trapped electron counts are similar to the variations in NAA amplitude shown at the top, suggesting that when the trapped fluxes are high there is a correspondingly larger precipitation flux of electrons at the same time. The second, later, dashed line also indicates that there was an increase in the POES >100 keV trapped flux at the same time as the change in NAA amplitude even though the change in A_p was barely noticeable around this time.

[15] Figure 5 shows that although A_p can be used to broadly indicate when electron precipitation is likely to occur, it fails to identify how long the effect would last and what precipitation flux levels into the atmosphere are likely to be generated. As such, it is not clear A_p is a good proxy

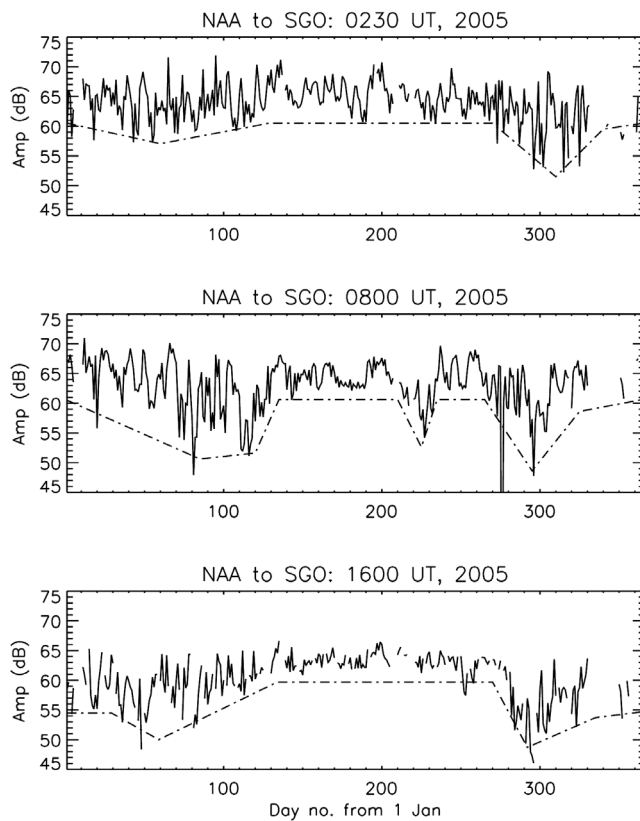


Figure 3. The variation of the amplitude of NAA received at Sodankylä for three 1 h time periods during 2005 (solid line). The times represent the MLT midnight sector (0230 UT), the morning sector (0800 UT), and the afternoon sector (1600 UT). The dash-dotted line represents the variation of quiet time amplitude values during the year, based on the analysis of data from 2005 to 2008. See text for more details.

to represent accurately energetic electron precipitation inside atmospheric models.

4. Calculating the Electron Precipitation Flux From NAA Amplitudes

[16] In this section, we model the effect of precipitating electrons on the propagation conditions between NAA and SGO. Ultimately, we use the amplitude changes of NAA to determine a flux level of precipitating electrons for each observation of NAA amplitude during the time periods studied. Inherent in this calculation is the need to know what the electron precipitation spectrum is and to show that the received NAA amplitude changes consistently in direct correspondence with the precipitation flux changes. The details of these calculations and assumptions are discussed in the following text.

[17] Although POES can give us some idea of the time variation of electron fluxes the detectors are unable to provide accurate knowledge of the energy spectrum of the precipitating electrons because of the wide energy range covered by the detectors (i.e., >30 keV, >100 keV, >300 keV), along with the varying impact of low-energy proton contamination

in each of these electron energy channels [Rodger *et al.*, 2010]. However, the DEMETER satellite carries an electron detector that has good energy resolution and monitors electrons in the drift loss cone up to $L \sim 7$. In Figure 6, we show a typical example of the average $L = 3-7$ energy spectrum observed by DEMETER in 2005. We undertake fitting the spectrum from ~ 90 to 700 keV in terms of a power law where the slope (scaling exponent, k) is -2 . We limit ourselves to an upper range of 700 keV in order to take account of some periods in the DEMETER data when it is unclear that the energy spectra are well represented by a power law relationship, such as the feature that shows increasing flux at ~ 2 MeV in Figure 6. Longer-term, annual averages, over the range $L = 3-7$ (equivalent to the L shell coverage of the whole NAA-SGO path), indicate that the energy spectral gradient has a power law slope of -2 ± 1 . We use this average value later in the paper to provide some spectral gradient information about the precipitating electrons. In Figure 6, the dashed and dot-dashed lines represent the typical energy spectra that produce the values of $k = -3$ and $k = -1$, respectively, and indicate the range of energy spectra observed by DEMETER in 2005 averaged over $L = 3-7$.

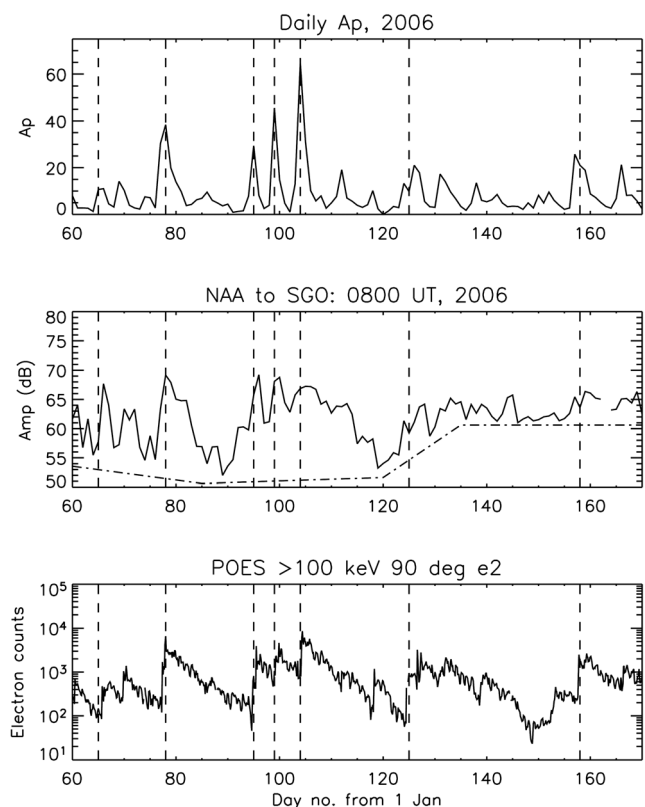


Figure 4. The variation in (top) daily A_p , (middle) NAA amplitude, and (bottom) POES >100 keV trapped electron counts averaged over $L = 3-7$ from day 60 to day 170 (2006). Vertical dashed lines are plotted to highlight examples of geomagnetic storm periods as defined by A_p and their corresponding signatures in NAA amplitudes and POES electron counts.

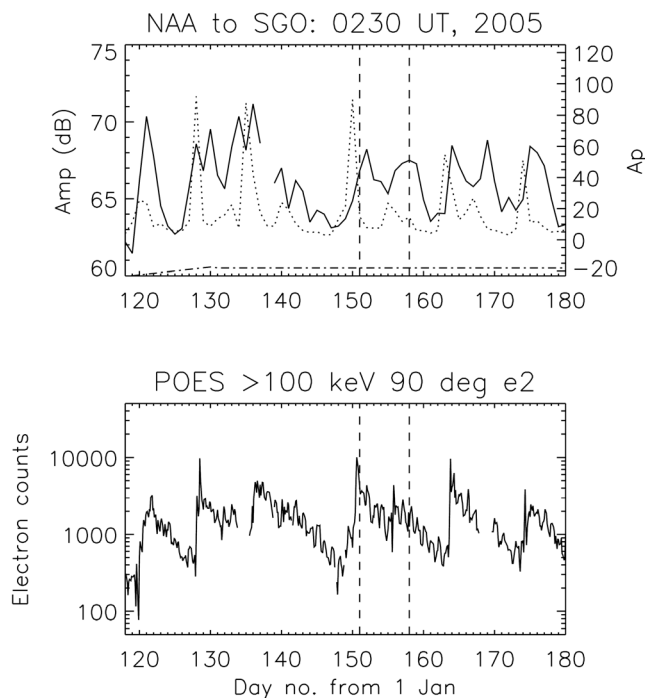


Figure 5. (top) The variation of NAA amplitude (solid line) during days 118–180 (2005) at 0230 UT compared with daily Ap (dotted line). The quiet time baseline values for NAA at this time of year are indicated by the dot-dashed line. (bottom) The POES >100 keV trapped electron counts (average over $L = 3-7$) during the same period as Figure 5 (top).

[18] While the POES telescopes provide BLC flux measurements, the issues of contamination, poor energy resolution, and unclear energy response mean that these measurements are very poorly suited to provide spectral gradient information for BLC precipitation. In contrast, DEMETER IDP measurements provide very well resolved energy spectra, and the POES problem with low-energy proton contamination in electron measurements [e.g., *Rodger et al.*, 2010] has not been reported in the DEMETER IDP observations. While DEMETER provides observations of the DLC rather than BLC, the wave-particle interactions that populate the DLC from the trapped fluxes will also be driving electrons into the BLC, and thus the BLC energy spectrum should be strongly related to that of the DLC. In this paper, we assume a constant energy spectrum in order to find the precipitation flux associated with each geomagnetic storm period. In a later publication, we plan to use the DEMETER data to develop a model of the behavior of the energy spectrum as a consequence of geomagnetic activity and use that to refine the determination of the precipitating fluxes.

[19] Using the electron energy spectrum shown in Figure 6 based on DEMETER drift loss cone measurements over the L shell range 3–7, we calculate the response of the NAA signal amplitude received at SGO. To do this, we calculate VLF/LF wave propagation of NAA to SGO using the Long Wave Propagation Code (LWPC) [*Ferguson and Snyder*, 1990]. LWPC models VLF signal propagation from any

point on Earth to any other point. Given electron density profile parameters for the upper boundary conditions, LWPC calculates the expected amplitude and phase of the VLF signal at the reception point. For undisturbed time periods, the D region electron density altitude profile is often expressed through a Wait ionosphere, defined in terms of a sharpness parameter β and a reference height h' [*Wait and Spies*, 1964], and the electron number density (i.e., electrons per m^{-3}) N_e increases exponentially with altitude z . We assume that the whole path is affected by excess ionization in the energy range 50 keV to 3 MeV on top of the underlying ionosphere defined by $\beta = 0.30 \text{ km}^{-1}$ and $h' = 74 \text{ km}$. These quiet time values of β and h' reproduce the nondisturbed amplitudes of NAA received at SGO for a high proportion of the year and local time (see Figure 3, i.e., 60.5 dB) and are consistent with the β and h' values suggested by *McRae and Thomson* [2000] for daytime propagation conditions.

[20] The ionization rate due to precipitating energetic electrons is calculated by an application of the expressions by *Rees* [1989] expanded to higher energies based on *Goldberg and Jackman* [1984]. The background neutral atmosphere is calculated using the NRLMSISE-00 neutral atmospheric model [*Picone et al.*, 2002]. We then use a model to describe the balance of electron number density in

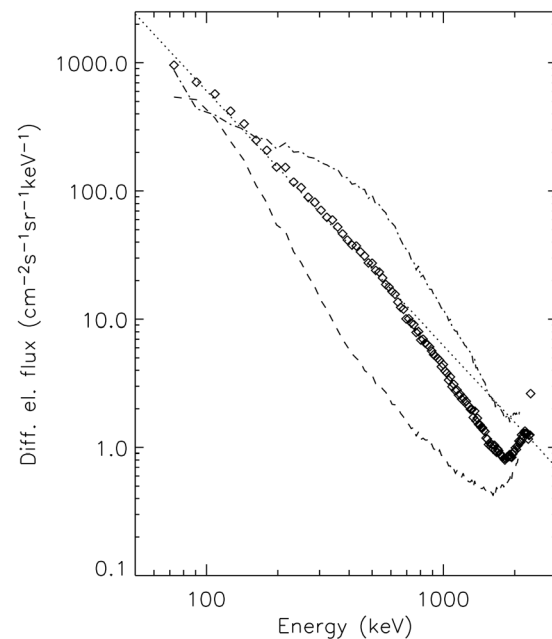


Figure 6. An example of the typical energy spectrum observed by DEMETER in the drift-loss cone on day 142 (2005) for $L = 3-7$ (diamonds). We undertake fitting the spectrum from ~ 90 to 700 keV. The fit is shown as a dotted line. The energy spectrum shown is representative of the annual average spectral gradient observed between 90 and 700 keV when averaging from $L = 3-7$. We note the presence of one very high flux value near 2 MeV but are unsure of its origin. Dot-dashed and dotted lines represent the energy spectra for the values of $k = -1$ and $k = -3$, respectively, and indicate the range of energy spectra observed by DEMETER in 2005 averaged over $L = 3-7$.

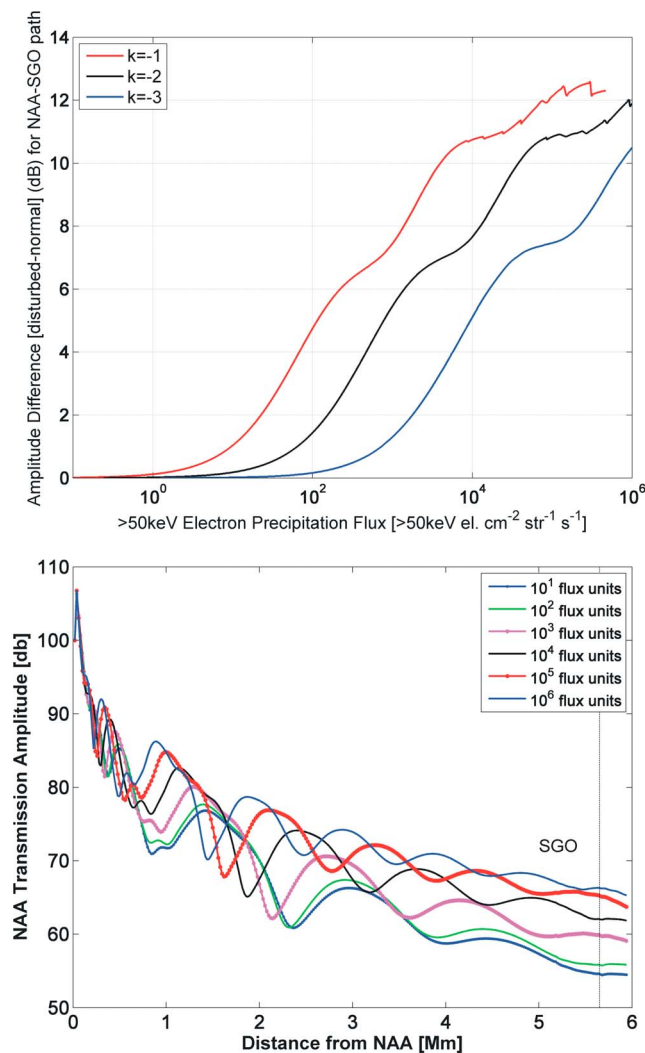


Figure 7. (top) The change in modeled amplitude of NAA received at SGO with increasing precipitation flux. The results of using different energy spectra of the precipitation flux are plotted, where the power law scaling exponent was varied from $k = -1$ to $k = -3$ (see text for more details). (bottom) The variation of NAA amplitude with distance from the transmitter, when influenced by a range of precipitation fluxes with energy spectral scaling exponent, $k = -2$. The location of SGO is shown.

the lower ionosphere based on that given by *Rodger et al.* [1998]. In this model, the evolution of the electron density in time is governed by the equation

$$\frac{\partial N_e}{\partial t} = q - \beta N_e - \alpha N_e^2, \quad (1)$$

where q is the ionization rate, α is the recombination coefficient ($\text{m}^3\text{ s}^{-1}$), and β is the attachment rate (s^{-1}). *Rodger et al.* [1998] provides expressions for the altitude variation of α and β . A more detailed description of the application of the simple model to investigate electron precipitation conditions is provided by *Rodger et al.* [2007b]. The electron number density profiles determined for varying

precipitation flux magnitudes are used as input to the LWPC subionospheric propagation model, thus modeling the effect of precipitation on the NAA received amplitudes at Sodankylä.

[21] In Figure 7 (top), we calculate the change in amplitude of NAA received at SGO as the precipitation flux along the whole path is uniformly increased, keeping the energy spectral gradient the same at all times. This approach effectively assumes that the precipitation flux is constant as a function of L . The plot shows the change in the amplitude of NAA with flux for three different cases of spectral gradient varying around the value of the power law scaling exponent (defined here as k) = -2 that we ultimately show results for later in this paper. Generally, it can be seen that the amplitude of the perturbation to NAA increases smoothly with increasing flux. This is a really important result for our analysis, as it shows that we are able to use a given NAA perturbation value to calculate a unique flux value (assuming a constant energy spectrum). At >50 keV flux levels below 10^1 $\text{el. cm}^{-2}\text{ s}^{-1}\text{ sr}^{-1}$ the modeled perturbation of the NAA amplitude is too small to be reliably determined in the observations. The maximum modeled deviations of NAA amplitudes from the baseline are ~ 9 – 10 dB, suggesting that the typical flux range capable of being detected by this technique is 10^1 – 10^5 $\text{el. cm}^{-2}\text{ s}^{-1}\text{ sr}^{-1}$.

[22] In Figure 7 (bottom), we show the NAA amplitude variation with distance between NAA and SGO. The colored lines represent factors of 10 changes in precipitating flux levels and show the effects that the precipitation has on propagation along the path up to and just beyond the distance of SGO. The oscillating characters of the lines shown in this plot are a result of modal interference causing amplitude fading. In this frame, the spectral slope was kept constant ($k = -2$). The plot shows that at the distance of SGO increases in precipitation flux produce well-ordered increases in NAA amplitude, whereas at many other distances the relationship between precipitation flux and amplitude change is much more complex, indicating that the location of SGO is particularly suitable for the study undertaken in this paper.

[23] Using the spectral gradient results shown in Figure 7 (top; black line, $k = -2$), we can calculate the equivalent precipitation flux for NAA amplitude values that exceed the normal quiet time level of 60.5 dB. We chose here to express the electron precipitation flux in terms of the integral flux of electrons >100 keV $\text{cm}^{-2}\text{ s}^{-1}\text{ sr}^{-1}$, with an upper limit of 3 MeV. Using a spectral gradient of $k = -2$ means that the integral flux of electrons >100 keV $\text{cm}^{-2}\text{ s}^{-1}\text{ sr}^{-1}$ is 50% of the >50 keV $\text{cm}^{-2}\text{ s}^{-1}\text{ sr}^{-1}$ flux calculated in Figure 7. The results shown in Figure 8 compare the variation of the calculated integral flux based on NAA amplitudes on days 100–250 (2005), with the integral flux of >100 keV with an upper limit of 1 MeV $\text{cm}^{-2}\text{ s}^{-1}\text{ sr}^{-1}$ observed by DEMETER in the drift loss cone during the same period, and the POES >100 keV $\text{cm}^{-2}\text{ s}^{-1}\text{ sr}^{-1}$ “trapped” flux (90° detector) and loss flux (0° detector) converted from counts to flux using the geometric factor of 100 suggested by *Evans and Greer* [2004]. Although they are less likely to precipitate into the atmosphere than “loss” fluxes, we show POES “trapped” fluxes here in order to provide some indication of the maximum flux available for

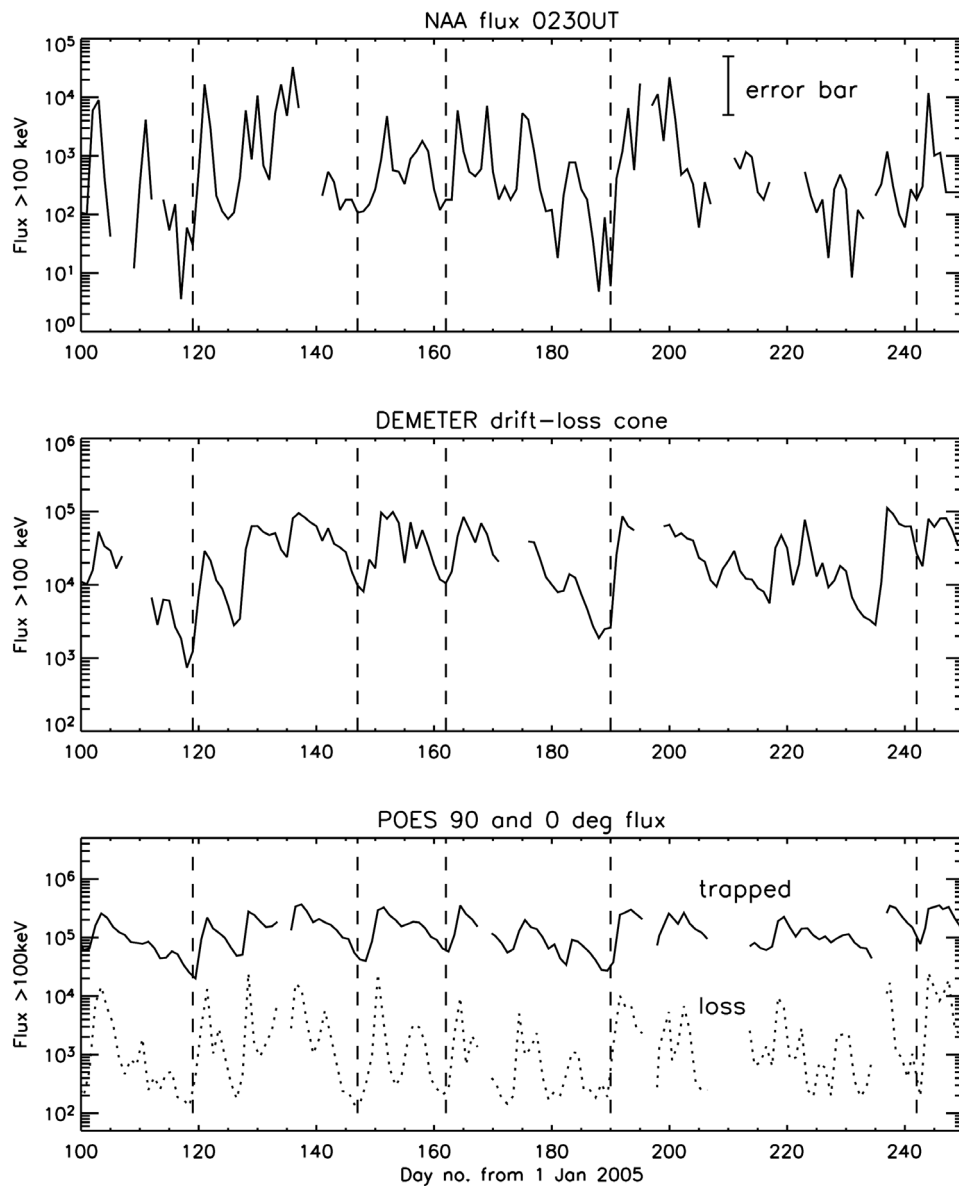


Figure 8. A comparison between (top) the variation of the >100 keV flux determined from the NAA amplitude at 0230 UT in days 100–250 (2005), (middle) the >100 keV electron flux observed by DEMETER in the drift loss cone, and (bottom) the POES “trapped” and “loss” fluxes >100 keV. All flux units are $\text{el. cm}^{-2} \text{s}^{-1} \text{sr}^{-1}$. The DEMETER and POES fluxes are an average of $L = 3$ –7. See text for more details. Vertical dashed lines indicate the times when both data series show sudden enhancements associated with geomagnetic storms.

precipitation. We would not expect the NAA flux levels to exceed the POES “trapped” flux levels at any time. The NAA flux panel shows a factor of 10 error bar, which represents the uncertainty on the flux estimate introduced by using a fixed spectral gradient factor. The DEMETER and POES fluxes are an average across $L = 3$ –7. The DEMETER fluxes are shown as an average of all longitudes (solid line). Vertical dashed lines indicate the times when both data series show sudden enhancements associated with geomagnetic storms.

[24] Figure 8 indicates that there is good correspondence between the instruments in terms of showing elevated electron fluxes in the trapped, drifting, and precipitating

environments at the same time and similarly coincident periods of low fluxes. However, there are clearly some differences that are apparent at times, e.g., about day 120 when the POES “trapped” fluxes increase by an order of magnitude or so along with the DEMETER drift loss cone flux, the POES loss flux increases by 2 orders of magnitude, and the precipitating fluxes (determined from NAA) increase by 3 orders of magnitude. However, at other times, there is good agreement between the variation in POES fluxes, DEMETER drift loss cone flux variations, and the precipitating flux variations (e.g., days 140–175).

[25] The large variation of energetic electron precipitation fluxes shown in Figure 8 could be driven by multiple

radiation belt processes, such as acceleration and loss by several different VLF wave-particle interaction processes [Imhof *et al.*, 1992; Blake *et al.*, 1996; Millan *et al.*, 2002; Horne, 2002], and radial transport by ULF waves [Mathie and Mann, 2000; Fei *et al.*, 2006, and references therein]. Gyroresonant pitch angle scattering of electrons by chorus, plasmaspheric hiss, and EMIC waves can lead to significant precipitation into the atmosphere and net loss of energetic electrons from the outer radiation belt [e.g., Lorentzen *et al.*, 2001; O'Brien *et al.*, 2004; Thorne *et al.*, 2005; Rodger *et al.*, 2007a, 2008]. Radiation belt electron precipitation has also been shown to be longer lasting during recurrent high-speed solar wind stream storms (HSSWS) than during coronal mass ejections (CMEs) [Longden *et al.*, 2008]. However, the detailed time variability, energy spectrum, and flux have proved difficult to measure.

[26] Finally, using the three time periods of magnetic midnight (0230 UT at SGO or 22–06 MLT on the propagation path), morning sector (0800 UT at SGO or 0330–1130 MLT on the path), and afternoon sector (1600 UT at SGO or 1130–1930 MLT on the path), we compare the precipitating fluxes determined from NAA at different MLT for a single storm event. Figure 9 shows the estimated integral >50 keV precipitation flux following a geomagnetic storm that started on 9 July 2005 and reached a maximum of $K_p = 6+$ on 12 July 2005. The largest fluxes were measured in the postmidnight sector (solid line), with the premidnight sector showing slightly lower fluxes (dotted line), and the noon sector fluxes the lowest (dot-dashed line). Data gaps are caused either by the transmitter being off-air for some time or when recordings were interrupted. In all three time sectors, the integral fluxes remain elevated from the start of the storm on day 190 until at least day 205.

5. Discussion

[27] In section 3 and Figures 3–5 and 8, we showed that the amplitude of NAA received at SGO increased in amplitude during periods of geomagnetic activity, and there was good correspondence with the variation of POES electron fluxes. From these figures, we were able to confirm that the NAA amplitude variation can be used to identify periods of electron precipitation, particularly when concentrating on well-defined times associated with specific MLT zones such as midnight (0230 UT).

[28] One key area for discussion, highlighted by Figures 3–5, is that the perturbation magnitude of the NAA amplitude response to geomagnetic storms is different at different times of year. Also, the baseline conditions for all three study UT (MLT) periods vary throughout the year, although they are basically the same during the well-illuminated summer months (i.e., May–August). However, the maximum amplitudes exhibited by NAA during geomagnetic storms are typically the same at all times of year, with peak amplitudes reaching ~ 70 dB, i.e., about 9–10 dB above the summer time baseline value of 60.5 dB and about 20 dB above the occasional winter time baseline values of ~ 50 dB. This similarity in the seasonal peak amplitude response suggests that during winter time the NAA amplitudes are more responsive to very low level precipitating fluxes than during the summer time. But conversely, moderate to high-electron precipitation fluxes swamp the underling

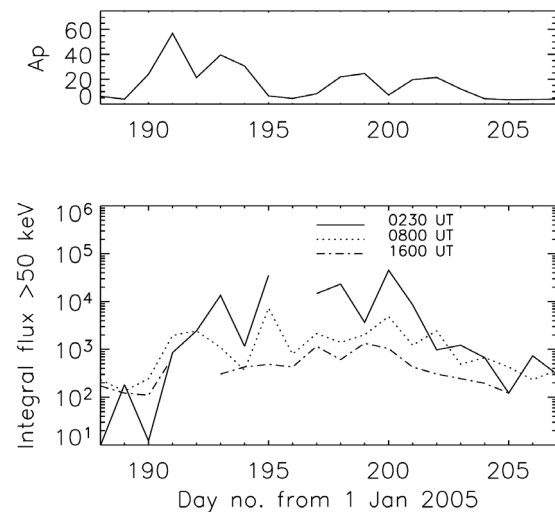


Figure 9. An example of the magnetic local time variation of the estimated integral >50 keV precipitation flux following a geomagnetic storm that started on 9 July 2005. The largest fluxes were measured in the midnight sector (0230 UT), with the morning sector showing slightly lower fluxes (0800 UT), and the afternoon sector fluxes the lowest (1600 UT). In all three time sectors, the integral fluxes remain elevated from the start of the storm on day 190 until day 205.

ionospheric density profile and produce the same NAA amplitudes whatever the time of year. Therefore, we could follow one of two approaches to modeling the response of NAA to electron precipitation at different times of the year: (1) by modeling the baseline ionospheric conditions at all times of the year and calculating the response of NAA to electron precipitation for all ionospheric conditions and (2) by modeling the NAA response to electron precipitation for the most common ionospheric condition seen, i.e., the summer time (days 130–210) when the baseline amplitude is ~ 60.5 dB. The second of these approaches effectively ignores any electron precipitation flux information that could be ascertained from NAA amplitudes below 60.5 dB, conditions which occur primarily in the winter time.

[29] Section 4 (Figures 6–7) uses the second approach to calculate the electron precipitation flux required to perturb the NAA amplitudes above the 60.5 dB level. The fact that the modeled NAA amplitudes increase smoothly with increasing precipitation flux is encouraging. In order to achieve these modeling results, two significant assumptions were made: (1) that the electron precipitation occurred uniformly over the whole propagation path and (2) that the electron precipitation spectrum had a constant power law scaling exponent value of $k = -2$. In reality, neither of these assumptions are likely to be completely accurate during a geomagnetic storm period. The spectral gradient is likely to vary in response to changing electron acceleration/loss processes in the outer radiation belt during storms, and those acceleration/loss processes are likely to vary with L shell (i.e., along the NAA propagation path).

[30] The results presented in this initial study represent analysis undertaken with the simplest, but reasonably typical, conditions that are likely to occur. In future studies, we will aim to include a spectral gradient model that changes with

geomagnetic activity level and L shell, allow for nonuniform precipitation over the propagation path, and include modeling that takes into account the underlying ionospheric conditions for different times of year. Ultimately, we aim to provide this analysis for all UT (MLT) periods of the day and with higher time resolution than the 1 h average that we currently analyze.

[31] In the latter part of section 4, we compare the calculated electron precipitation flux with those measured by the DEMETER satellite in the drift loss cone and the trapped/loss fluxes measured by POES. The energy ranges measured are typically >100 keV, with an upper limit of 1–3 MeV, although it would be expected that the highest fluxes of electrons would be at the lowest energies in a normal energy spectrum, and therefore, a comparison between the instruments is reasonable. Typically, when averaging over $L = 3$ –7, we find that the POES trapped fluxes peak at about 10^6 el. $\text{cm}^{-2} \text{s}^{-1} \text{sr}^{-1}$, with the DEMETER drift loss cone showing peak fluxes of 10^5 el. $\text{cm}^{-2} \text{s}^{-1} \text{sr}^{-1}$ and both the POES loss fluxes and the NAA precipitation fluxes showing peaks of $\sim 10^4$ el. $\text{cm}^{-2} \text{s}^{-1} \text{sr}^{-1}$. However, the NAA-based precipitating fluxes show larger dynamic range than the POES loss fluxes, with most of the differences between the two time series occurring at the lowest fluxes. At quiet geomagnetic times, the ground-based NAA precipitation fluxes can be an order of magnitude lower than POES loss fluxes, which reflects the sensitivity limit of the POES instrument ($\sim 10^2$ el. $\text{cm}^{-2} \text{s}^{-1} \text{sr}^{-1}$) once the precipitation fluxes become very small. However, the comparison with POES loss fluxes is likely to be refined by planned improvements in the NAA flux calculations, such as incorporating the energy spectrum model, which could introduce changes of factors of ± 10 as indicated by the error bar in Figure 7 (top).

[32] Finally, a word of warning. The comparison of the absolute values of NAA and POES precipitating fluxes shown in Figure 8 should be taken as a guide only. The fluxes determined from NAA amplitude perturbations are a best estimate of the precipitating fluxes, i.e., they represent the whole of the bounce loss cone which precipitates into the atmosphere. In contrast, the $L = 3$ –7 POES loss fluxes are observed at L shells where the detector angle is considerably smaller than the bounce loss cone angle. An accurate conversion of POES loss fluxes to precipitation flux would require a knowledge of the detector view relative to the loss cone angle (e.g., edge or middle) and the pitch angle distribution of the fluxes in the loss cone. This means that although we can say that the POES precipitation fluxes are likely to be underestimated in Figure 8, it would be very difficult to say by exactly how much. Further work is required to provide a detailed comparison between the NAA precipitation fluxes and the POES precipitation fluxes, primarily through fine tuning the NAA precipitation flux technique as discussed above.

6. Summary

[33] We have used AARDDVARK data from a radio wave receiver in Sodankylä, Finland to monitor transmissions from the very low frequency naval transmitter, NAA, in Cultler, Maine, USA since 2004. The transmissions from NAA

(24.0 kHz, 44°N, 67°W, $L = 2.9$) received at Sodankylä (SGO, 67°N, 26°E, $L = 5.1$) are influenced by energetic particle precipitation between $L = 3$ –7, i.e., the outer radiation belt. By modeling the effect of electron precipitation on the subionospherically propagating NAA signals, using electrons with energies between 50 keV and 3 MeV, we have been able to show that the observed amplitude variations can be used to determine the flux of energetic electrons entering the atmosphere through processes occurring in the radiation belts.

[34] Analysis of NAA observations, particularly in 2005–2006, has shown that ground-based electron precipitation fluxes can vary by 3 orders of magnitude during geomagnetic storms. For some geomagnetic storms, the precipitation level is well represented by a geomagnetic proxy such as A_p , but there are also occasions where significant precipitation occurs without enhanced A_p levels and occasions where precipitation continues after A_p has returned to quiet time levels following a storm. A_p may be useful to specify the onset of particle precipitation but not the amount or duration of the precipitation itself.

[35] Comparison of the ground-based precipitation flux variations with satellite observations from DEMETER and POES shows a broad agreement during geomagnetic storms but some differences in the quiet time levels, with the satellites reporting higher fluxes than those observed from the ground. Typically when averaging over $L = 3$ –7, we find that the POES “trapped” fluxes peak at about 10^6 el. $\text{cm}^{-2} \text{s}^{-1} \text{sr}^{-1}$ during geomagnetic storms, with the DEMETER drift loss cone showing peak fluxes of 10^5 el. $\text{cm}^{-2} \text{s}^{-1} \text{sr}^{-1}$, and both the POES “loss” fluxes and the NAA precipitation fluxes showing peaks of $\sim 10^4$ el. $\text{cm}^{-2} \text{s}^{-1} \text{sr}^{-1}$.

[36] While we have only examined some MLT periods for variability in this study, we have been able to show that during a geomagnetic storm in July 2005 the electron precipitation flux pre-midnight exceeded the fluxes from the post-midnight side and also from the noon sector. The ground-based analysis of NAA amplitude variability has the potential of providing a detailed local time picture of electron precipitation fluxes.

[37] In this study, we have introduced the possibility of being able to routinely determine the electron precipitation flux into the atmosphere from a ground-based experiment and potentially in near real time. In order to determine the fluxes, we have had to make some assumptions about the characteristics of the precipitation: assuming uniform precipitation over the whole NAA-SGO propagation path and assuming an unchanging energy spectral gradient. In future work, we aim to address these limitations of the analysis undertaken here through additional modeling efforts and by combining AARDDVARK data from other transmitter-receiver propagation paths.

[38] **Acknowledgments.** The collection, analysis, and interpretation of AARDDVARK data have been supported by funding from the Finnish Academy. We would also like to acknowledge the funding of the LAPBIAT2 program (contract RITA-CT-2006-025969). The work of A.S. was supported by the EPPIC Marie Curie FP7 project (PIEF-GA-2009-237461). The work of J.A.S. and M.P. was supported by the Centre National d’Etudes Spatiales (CNES). C.J.R. is a Guest Investigator inside the DEMETER program.

[39] Robert Lysak thanks Jan Wissing and Michael Rycroft for their assistance in evaluating this paper.

References

- Adams, C. D. D., and R. L. Dowden (1990), VLF group delay of lightning-induced electron-precipitation echoes from measurement of phase and amplitude perturbations at 2 frequencies, *J. Geophys. Res.*, *95*(A3), 2457–2462, doi:10.1029/JA095iA03p02457.
- Barr, R., D. L. Jones, and C. J. Rodger (2000), ELF and VLF radio waves, *J. Atmos. Sol. Terr. Phys.*, *62*, 1689–1718.
- Baumgaertner, A. J. G., P. Jöckel, and C. Brühl (2009), Energetic particle precipitation in ECHAM5/MESy1: Part 1. Downward transport of upper atmospheric NO_x produced by low energy electrons, *Atmos. Chem. Phys.*, *9*, 2729–2740.
- Blake, J. B., M. D. Looper, D. N. Baker, R. Nakamura, B. Klecker, and D. Hovestadt (1996), New high temporal and spatial resolution measurements by SAMPEX of the precipitation of relativistic electrons, *Adv. Space Res.*, *18*(8), 171–186.
- Clilverd, M. A., N. R. Thomson, and C. J. Rodger (1999), Sunrise effects on VLF signals propagating over a long north-south path, *Radio Sci.*, *34*, 939–948.
- Clilverd, M. A., C. J. Rodger, and T. Ulich (2006), The importance of atmospheric precipitation in storm time relativistic electron flux dropouts, *Geophys. Res. Lett.*, *33*(1), L01102, doi:10.1029/2005GL024661.
- Clilverd, M. A., et al. (2009a), Remote sensing space weather events: The AARDDVARK network, *Space Weather*, *7*, S04001, doi:10.1029/2008SW000412.
- Clilverd, M. A., A. Seppälä, C. J. Rodger, M. G. Mlynczak, and J. U. Kozyra (2009b), Additional stratospheric NO_x production by relativistic electron precipitation during the 2004 spring NO_x descent event, *J. Geophys. Res.*, *114*, A04305, doi:10.1029/2008JA013472.
- Evans, D. S., and M. S. Greer (2004), Polar Orbiting environmental satellite space environment monitor: 2. Instrument descriptions and archive data documentation, NOAA Tech. Memo., ver. 1.4, Space Environ. Lab., Colo.
- Fei, Y., A. A. Chan, S. R. Elkington, and M. J. Wiltberger (2006), Radial diffusion and MHD particle simulations of relativistic electron transport by ULF waves in the September 1998 storm, *J. Geophys. Res.*, *111*, A12209, doi:10.1029/2005JA011211.
- Ferguson, J. A., and F. P. Snyder (1990), Computer programs for assessment of long wavelength radio communications, *Tech. Doc. 1773*, Natl. Ocean Syst. Cent., San Diego, Calif.
- Goldberg, R. A., and C. H. Jackman (1984), Nighttime auroral energy deposition in the middle atmosphere, *J. Geophys. Res.*, *89*(A7), 5581–5596, doi:10.1029/JA089iA07p05581.
- Horne, R. B. (2002), The contribution of wave-particle interactions to electron loss and acceleration in the Earth's radiation belts during geomagnetic storms, in *URSI Review of Radio Science 1999–2002*, edited by W. R. Stone, pp. 801–828, Wiley, New York.
- Horne, R. B., et al. (2005), Wave acceleration of electrons in the Van Allen radiation belts, *Nature*, *437*, 227–230.
- Imhof, W. L., R. M. Robinson, H. L. Collin, J. R. Wygant, and R. R. Anderson (1992), Simultaneous measurements of waves and precipitating electrons in the outer radiation belt, *Geophys. Res. Lett.*, *19*(24), 2437–2440, doi:10.1029/92GL02636.
- Longden, N., M. H. Denton, and F. Honary (2008), Particle precipitation during ICME-driven and CIR-driven geomagnetic storms, *J. Geophys. Res.*, *113*, A06205, doi:10.1029/2007JA012752.
- Lorentzen, K., M. Looper, and J. Blake (2001), Relativistic electron microbursts during the GEM storms, *Geophys. Res. Lett.*, *28*(13), 2573–2576, doi:10.1029/2001GL012926.
- Mathie, R. A., and I. R. Mann (2000), A correlation between extended intervals of ULF wave power and storm time geosynchronous relativistic electron flux enhancements, *Geophys. Res. Lett.*, *27*(20), 3261–3264, doi:10.1029/2000GL003822.
- McRae, W. M., and N. R. Thomson (2000), VLF phase and amplitude: Daytime ionospheric parameters, *J. Atmos. Sol. Terr. Phys.*, *62*(7), 609–618.
- Millan, R. M., R. P. Lin, D. M. Smith, K. R. Lorentzen, and M. P. McCarthy (2002), X-ray observations of MeV electron precipitation with a balloon-borne germanium spectrometer, *Geophys. Res. Lett.*, *29*(24), 2194, doi:10.1029/2002GL015922.
- O'Brien, T. P., M. D. Looper, and J. B. Blake (2004), Quantification of relativistic electron microburst losses during the GEM storms, *Geophys. Res. Lett.*, *31*, L04802, doi:10.1029/2003GL018621.
- Picone, J. M., A. E. Hedin, D. P. Drob, and A. C. Aikin (2002), NRLMSISE-00 empirical model of the atmosphere: Statistical comparisons and scientific issues, *J. Geophys. Res.*, *107*(A12), 1468, doi:10.1029/2002JA009430.
- Randall, C. E., et al. (2005), Stratospheric effects of energetic particle precipitation in 2003–2004, *Geophys. Res. Lett.*, *32*, L05802, doi:10.1029/2004GL022003.
- Rees, M. H. (1989), *Physics and Chemistry of the Upper Atmosphere*, Cambridge Univ. Press, Cambridge, U.K.
- Reeves, G. D. (1998), Relativistic electrons and magnetic storms: 1992–1995, *Geophys. Res. Lett.*, *25*(11), 1817, doi:10.1029/98GL01398.
- Rodger, C. J., and M. A. Clilverd (2008), Magnetospheric physics: Hiss from the chorus, *Nature*, *452*(7183), 41–42, doi:10.1038/452041a.
- Rodger, C. J., O. A. Molchanov, and N. R. Thomson (1998), Relaxation of transient ionization in the lower ionosphere, *J. Geophys. Res.*, *103*(A4), 6969–6975.
- Rodger, C. J., M. A. Clilverd, D. Nunn, P. T. Verronen, J. Bortnik, and E. Turunen (2007a), Storm time, short-lived bursts of relativistic electron precipitation detected by subionospheric radio wave propagation, *J. Geophys. Res.*, *112*, A07301, doi:10.1029/2007JA012347.
- Rodger, C. J., M. A. Clilverd, N. R. Thomson, R. J. Gamble, A. Seppälä, E. Turunen, N. P. Meredith, M. Parrot, J. A. Sauvaud, and J.-J. Berthelier (2007b), Radiation belt electron precipitation into the atmosphere: Recovery from a geomagnetic storm, *J. Geophys. Res.*, *112*, A11307, doi:10.1029/2007JA012383.
- Rodger, C. J., T. Raita, M. A. Clilverd, A. Seppälä, S. Dietrich, N. R. Thomson, and T. Ulich (2008), Observations of relativistic electron precipitation from the radiation belts driven by EMIC waves, *Geophys. Res. Lett.*, *35*, L16106, doi:10.1029/2008GL034804.
- Rodger, C. J., M. A. Clilverd, J. Green, and M.-M. Lam (2010), Use of POES SEM-2 observations to examine radiation belt dynamics and energetic electron precipitation in to the atmosphere, *J. Geophys. Res.*, *115*, A04202, doi:10.1029/2008JA014023.
- Roazanov, E., et al. (2005), Atmospheric response to NO_y source due to energetic electron precipitation, *Geophys. Res. Lett.*, *32*, L14811, doi:10.1029/2005GL023041.
- Sauvaud, J. A., T. Moreau, R. Maggiolo, J.-P. Treilhou, C. Jacquy, A. Cros, J. Coutelier, J. Rouzaud, E. Penou, and M. Gangloff (2006), High-energy electron detection onboard DEMETER: The IDP spectrometer, description and first results on the inner belt, *Planet. Space Sci.*, *54*(5), 502–511.
- Seppälä, A., C. E. Randall, M. A. Clilverd, E. Roazanov, and C. J. Rodger (2009), Geomagnetic activity and polar surface level air temperature variability, *J. Geophys. Res.*, *114*, A10312, doi:10.1029/2008JA014029.
- Thorne, R. M., T. P. O'Brien, Y. Y. Shprits, D. Summers, and R. B. Horne (2005), Timescale for MeV electron microburst loss during geomagnetic storms, *J. Geophys. Res.*, *110*, A09202, doi:10.1029/2004JA010882.
- Wait, J. R., and K. P. Spies (1964), Characteristics of the Earth-ionosphere waveguide for VLF radio waves, *NBS Tech. Note 300*, Natl. Inst. of Stand. and Technol., Gaithersburg, Md.

M. A. Clilverd and A. Seppälä, British Antarctic Survey, Natural Environment Research Council, High Cross, Madingley Road, Cambridge CB3 0ET, UK. (macl@bas.ac.uk; annika.seppala@bas.ac.uk)

R. J. Gamble, C. J. Rodger, and N. R. Thomson, Department of Physics, University of Otago, PO Box 56, Dunedin, New Zealand. (crodger@physics.otago.ac.nz; rgamble@physics.otago.ac.nz; n_thomson@physics.otago.ac.nz)

J. C. Green, NOAA Space Environment Center, 325 Broadway Blvd., Boulder, CO 80305, USA. (janet.green@noaa.gov)

M. Parrot, Laboratoire de Physique et Chimie de l'Environnement et de l'Espace, 3A Avenue de la Recherche Scientifique, 45071 Orleans CEDEX 2, France. (mparrot@cnsr-orleans.fr)

T. Raita and T. Ulich, Sodankylä Geophysical Observatory, University of Oulu, Sodankylä, Finland. (tero.raita@sgo.fi; thu@sgo.fi)

J.-A. Sauvaud, Centre d'Etude Spatiale des Rayonnements, 9 Ave. du Colonel Roche 31028, Toulouse CEDEX 4, France. (sauvaud@cesr.fr)